

Enhancement of bone shadow region using local phase-based ultrasound transmission maps

Ilker Hacihaliloglu^{1,2}

Received: 25 January 2017 / Accepted: 6 March 2017 / Published online: 11 March 2017
© CARS 2017

Abstract

Purpose Ultrasound is increasingly being employed in different orthopedic procedures as an imaging modality for real-time guidance. Nevertheless, low signal-to-noise-ratio and different imaging artifacts continue to hamper the success of ultrasound-based procedures. Bone shadow region is an important feature indicating the presence of bone/tissue interface in the acquired ultrasound data. Enhancement and automatic detection of this region could improve the sensitivity of ultrasound for imaging bone and result in improved guidance for various orthopedic procedures.

Methods In this work, a method is introduced for the enhancement of bone shadow regions from B-mode ultrasound data. The method is based on the combination of three different image phase features: local phase tensor, local weighted mean phase angle, and local phase energy. The combined local phase image features are used as an input to an L_1 norm-based contextual regularization method which emphasizes uncertainty in the shadow regions. The enhanced bone shadow images are automatically segmented and compared against expert segmentation.

Results Qualitative and quantitative validation was performed on 100 in vivo US scans obtained from five subjects by scanning femur and vertebrae bones. Validation against expert segmentation achieved a mean dice similarity coefficient of 0.88.

Conclusions The encouraging results obtained in this initial study suggest that the proposed method is promising

enough for further evaluation. The calculated bone shadow maps could be incorporated into different ultrasound bone segmentation and registration approaches as an additional feature.

Keywords Local phase · Local energy · Ultrasound · Segmentation · Bone · Enhancement

Introduction

Computer-assisted orthopedic surgery (CAOS) systems have been incorporated into various procedures ranging from total hip replacement (THR) [23], total knee replacement (TKR) [37], intramedullary nail locking for femoral shaft fractures [38] to pedicle screw insertion for spinal fusion surgeries [28]. High accuracy, reduction in total surgery time, and reduced postoperative complications are some of the advantages of these systems. The dominant intra-operative imaging modality in most of the developed CAOS systems has been two-dimensional (2D) fluoroscopy. However, the representation of the three-dimensional (3D) bone anatomy with 2D planar scans necessitates the use of multiple fluoroscopy scans taken from different direction which has affected the accuracy and reproducibility of the surgical procedures. In order to overcome this problem and provide improved guidance, 3D fluoroscopy scanners (O-arm, Iso-C) have been developed [21, 29, 39, 41]. Nonetheless, the high cost of 3D fluoroscopy units limited their applicability in CAOS systems. Finally, one of the major concerns for 2D/3D fluoroscopy-based guidance has been the exposure of surgical team and patient to ionizing radiation.

In recent years, in order to decrease the total amount of radiation exposure and provide real-time guidance, researchers have tried to incorporate ultrasound (US) as an

✉ Ilker Hacihaliloglu
ilker.hac@soe.rutgers.edu

¹ Department of Biomedical Engineering, Rutgers University, Piscataway, NJ, USA

² Department of Radiology, Rutgers University Robert Wood Johnson Medical School, New Brunswick, NJ, USA

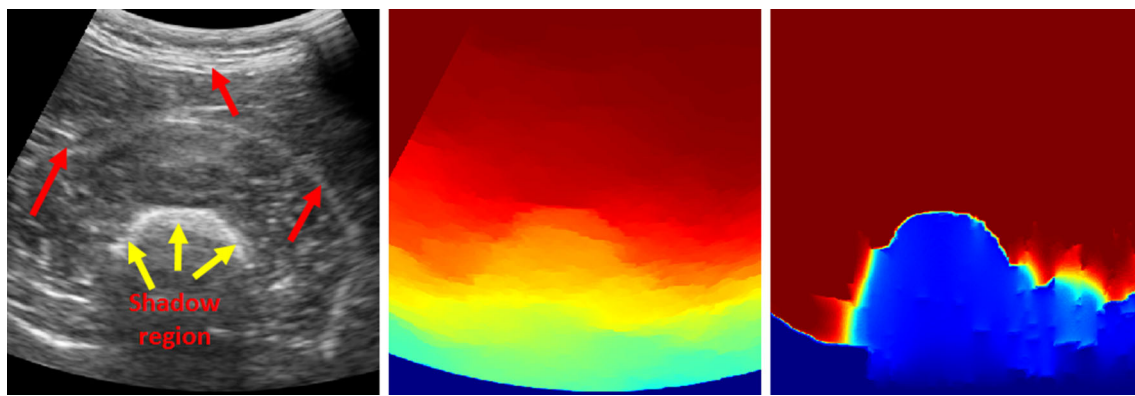


Fig. 1 *Left* B-mode US image of femur obtained *in vivo*. *Red* arrows point to soft tissue interfaces while *yellow* ones point to the expected bone surface. Shadow region is shown as the *dark* intensity region fol-

lowing the bone surface response. *Middle* shadow region detected using [25]. *Right* shadow region detected using the proposed method

intra-operative imaging modality into different CAOS procedures [1,4,5,8–10,18]. The main advantage of US is its real-time, 2D/3D, and non-radiation-based imaging capabilities. However, successful detection and extraction of bone surfaces from the collected scans still continue to be problematic due to high levels of noise and different imaging artifacts (Fig. 1). Due to the elevation beam width and being a user-dependent imaging modality regions corresponding to bone boundaries appear several mm in thickness and blurred further complicating the identification process [20,22]. In order to overcome some of these challenges, US bone segmentation [7,12,16,24,27,33,34,40] or bone enhancement [2,3,17,19] methods has been developed. Although successful results were reported, difficulty in acquiring US images with high-intensity bone boundaries is an ongoing limitation of current US-guided CAOS procedures.

One of the important features of bone US images is the shadow region. Once the US signal reaches a tissue–bone interface, due to the high acoustic impedance difference, most of the signal is reflected back resulting in a region with low-intensity values which is denoted as shadow region (Fig. 1). Automatic identification of shadow regions is important since it can be used as an additional feature to improve the robustness and accuracy of the segmentation or registration methods. Amin et al. [1] used the shadow region as an additional feature for their registration method. The proposed method detected the shadow region using an upward-tracing approach joined with intensity-based thresholding. Foroughi et al. [16] have incorporated bone shadow region as an additional feature for their bone segmentation method. Shadow region was identified using a weighted sum of intensity values obtained by masking the B-mode US image with a Gaussian function [16]. The same bone shadow detection method was also used as an additional feature for segmenting femur [24], spinous process [7], and wrist [3] bone surfaces. Yan et al. [40] selected image pixels above 20% of the maximum inten-

sity value for bone feature extraction. The extracted features were used for subsequent registration. In [25], the propagation of US signal was modeled using random walk-based image processing method. The resulting image, confidence map (CM), provided a probability measure of a random walk starting from a pixel to reach a virtual transducer under US-specific constraints. Since a pixel located inside the shadow region has a low probability reaching the virtual transducer elements this method provided a more robust shadow region detection and has been incorporated into different US bone segmentation methods [33,34]. Most of the previously proposed bone shadow detection methods are based on the use of US image intensity and/or gradient information. Therefore, the results remain unpredictable and are affected by the imaging conditions. Scans with shadow region artifacts or low-intensity blurred bone boundaries decreased the robustness of the intensity-based shadow region detection methods. Recently, the CM estimation approach was extended for processing radio frequency (RF) US signal [26]. Although improved results compared to the original CM method were achieved, access to RF signal data requires special hardware which is not readily available in most clinical US machines.

To overcome the previously explained problems and provide a more robust bone shadow detection, we propose a method where three different local phase image features are utilized together in order to enhance the appearance of bone surfaces from US data. The calculated local phase features are intensity invariant and provide a more robust feature representation compared to intensity-/gradient-based methods. We introduce a new US-specific signal transmission model obtained by incorporating the extracted bone features into a weighted L_1 norm-based contextual regularization method. During the final stage, the obtained transmission model is used for the enhancement of shadow regions. The particular clinical focus of this work is on fractures involving femoral shaft and the spine. Annual rate of femoral shaft fractures

in the USA alone is more than 60,000 [32]. According to a recent study, discharge rates for spinal fusion surgeries increased by 137% between the years 1998–2008 [35]. In both of these surgical procedures, high accuracy is necessary in order to avoid postsurgical complications. Furthermore, both of these procedures require high amounts of fluoroscopy usage time. Accordingly, the quantitative and qualitative validation results are presented on 100 in vivo femur and vertebrae US scans obtained from five healthy subjects.

Methods

The presented method is based on alteration of previously proposed US CM approach [25]. However, instead of using the US image intensity information, we use local phase image features in order to enhance the appearance of bone surfaces in the collected data. The enhanced images are used as an input to a new regularization method for improved modeling of US signal propagation. The final stage involves the enhancement of shadow regions using the calculated US signal propagation model. In the following sections, we first present the bone enhancement method, and then, we demonstrate how improved bone shadow detection can be obtained using our proposed regularization method.

Local-phase bone enhancement

The US response profile of a bone is highly correlated with the orientation of the transducer, with respect to the imaged surface, and the geometry of the imaged bone. In the context of our specific clinical focus while femur bone response behaves more like a dominant ridge edge along the scan-line direction, the spine bone response can be dominated by different response profiles due to the complex shape of the vertebrae and surrounding ligaments. Therefore, in order to provide a general enhancement method, we construct a tensor-based phase descriptor. Specifically, we calculate the local phase tensor (LPT(x, y)) image [19] using gradient energy tensor (GET) filter which provides a simultaneous estimation of local orientation and phase information [13]. The GET filter response is calculated as:

$$\text{GET}(\text{US}_{\text{DB}}(x, y)) = T_{\text{even}} + T_{\text{odd}} = \begin{bmatrix} \text{GET}_{11} & \text{GET}_{12} \\ \text{GET}_{21} & \text{GET}_{22} \end{bmatrix}$$

where

$$T_{\text{even}} = [\mathbf{H}(\text{US}_{\text{DB}}(x, y))] [\mathbf{H}(\text{US}_{\text{DB}}(x, y))]^T,$$

$$T_{\text{odd}} = -0.5 \times ([\nabla \text{US}_{\text{DB}}(x, y)] [\nabla \nabla^2 \text{US}_{\text{DB}}(x, y)]^T + [\nabla \nabla^2 \text{US}_{\text{DB}}(x, y)] [\nabla \text{US}_{\text{DB}}(x, y)]^T). \quad (1)$$

The first term T_{even} represents symmetric features, whereas the second term T_{odd} represents the asymmetric features. \mathbf{H} , ∇ and ∇^2 denote the Hessian, Gradient and Laplacian operations, respectively. $\text{US}_{\text{DB}}(x, y)$ represents a distance weighted and band-pass filtered US image. The distance weighting operation allows the masking out of erroneous regions, such as the soft tissue interface closer to the transducer surface, and improve the enhancement of bone surfaces located deeper in the image (Fig. 2b). Band-pass filtering was obtained using a Log-Gabor filter [19]. The LPT(x, y) image is calculated as $\text{LPT}(x, y) = \sqrt{T_{\text{even}}^2 + T_{\text{odd}}^2} \times \cos(\varphi)$. Here, φ represents the instantaneous phase obtained from the symmetric (T_{even}) and asymmetric (T_{odd}) features responses [19].

Investigating the LPT(x, y) image (Fig. 2) we can see that the GET filter results in an overall enhancement of soft tissue and bone interfaces. In order to provide a more compact bone representation with less soft tissue features, we calculate local phase energy (LPE(x, y)) and local weighted mean phase angle (LwPA(x, y)) image features. These two images are calculated using monogenic signal theory [14, 15]. The monogenic signal image is computed using vector-valued odd filter (Riesz filter) whose Fourier domain representation is:

$$H_1(u_1, u_2) = \frac{u_1}{\sqrt{u_1^2 + u_2^2}}, \quad H_2(u_1, u_2) = \frac{u_2}{\sqrt{u_1^2 + u_2^2}}. \quad (2)$$

Using the odd filter, the monogenic signal image ($\text{US}_{\text{M}}(x, y)$) is formed by combining the band-pass filtered LPT(x, y) image ($\text{LPT}_{\text{B}}(x, y)$) with the Riesz filtered components as:

$$\text{US}_{\text{M}}(x, y) = [\text{LPT}_{\text{B}}(x, y), \text{LPT}_{\text{B}}(x, y) * h_1(x, y), \text{LPT}_{\text{B}}(x, y) * h_2(x, y)]. \quad (3)$$

Here, $h_1(x, y)$ and $h_2(x, y)$ are the spatial domain representations of $H_1(u_1, u_2)$ and $H_2(u_1, u_2)$, respectively, and $*$ is convolution operator. For band-pass filter, we select α -scale space derivative quadrature filters (ASSD) which are shown to produce improved edge detection results on simulated US images [6]. The ASSD filter is defined as:

$$\text{ASSD}(\omega) = \begin{cases} n_c \omega^a \exp(-(\sigma \omega)^{2a}) & \omega \geq 0 \\ 0 & \text{otherwise} \end{cases}. \quad (4)$$

In the above equation, a is constant derivative parameter which is chosen to be $a > 1$ in order for the filters to satisfy the DC condition [6]. n_c is a unit normalization constant calculated from the filter α value, and σ is the filter α -scale parameter. The LPE(x, y) and LwPA(x, y) images are calculated using:

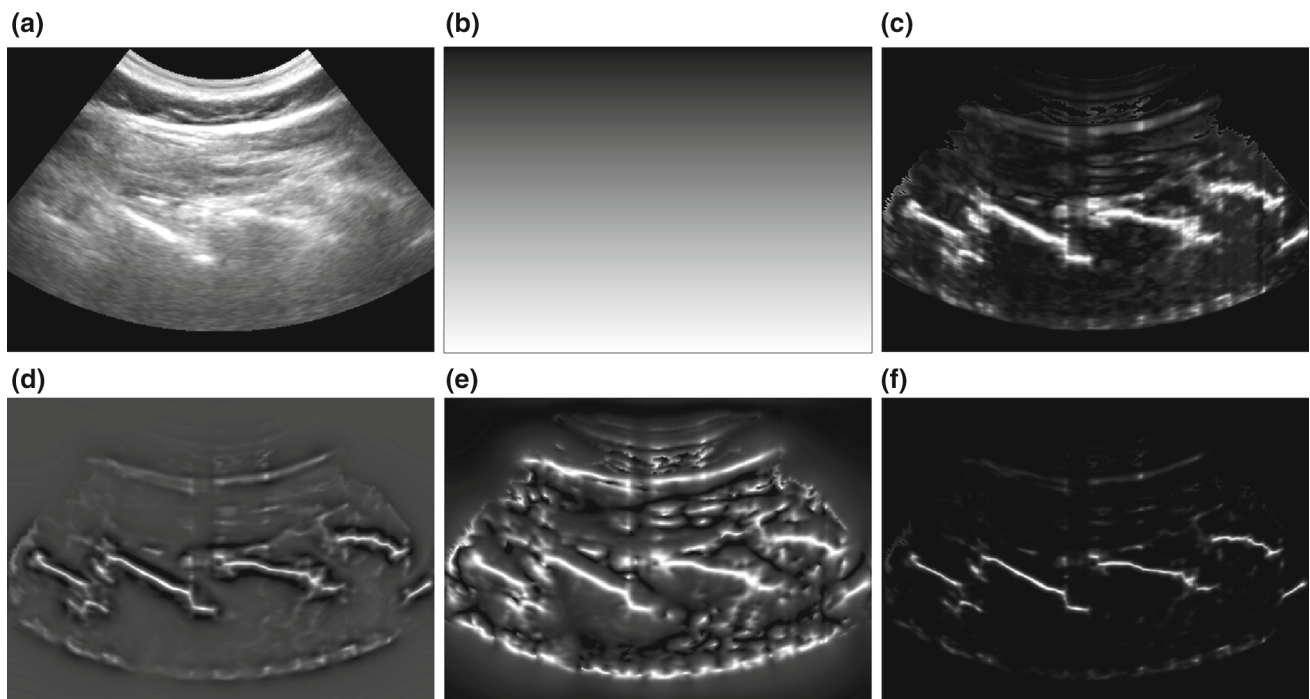


Fig. 2 **a** B-mode US image of spine obtained in vivo. **b** Distance map used during $LPT(x, y)$ image calculation. **c** $LPT(x, y)$ image. **d** $LPE(x, y)$ image. **e** $LwPA(x, y)$ image. **f** $LP(x, y)$ image obtained using a combination of **c–e**

$$LPE(x, y) = \sum_{sc} |US_{M1}(x, y)| - \sqrt{US_{M2}^2(x, y) + US_{M3}^2(x, y)}; \quad (5)$$

$$LwPA(x, y) = \arctan \left(\frac{\sum_{sc} US_{M1}(x, y)}{\sqrt{\sum_{sc} US_{M1}^2(x, y) + \sum_{sc} US_{M2}^2(x, y)}} \right). \quad (6)$$

In the above formulas, sc represents the number of scales. $LwPA(x, y)$ is a feature map image obtained by averaging the phase sum of the response vectors over many scales. This obtained feature map is noise independent. Consequently, noise compensation is not required and the $LwPA(x, y)$ image preserves all the structural details of the US image such as the soft tissue interfaces and bone surface. On the other hand, $LPE(x, y)$ image encodes the underlying shape of the bone boundary by accumulating the local energy of the image along several filter orientations. The final improved local phase bone image ($LP(x, y)$) is obtained using: $LP(x, y) = LPT(x, y) \times LPE(x, y) \times LwPE(x, y)$. Investigating the calculated $LPE(x, y)$ image (Fig. 2d), we can see that the dominant features extracted appear in the same location as the bone interfaces enhanced in the $LPT(x, y)$ image; however, they are more compact (thickness of the extracted boundary is thinner) and the soft tissue appearance is not as dominant. On the other hand, in the $LwPA(x, y)$ image (Fig. 2e),

the ridge edge features corresponding to bone and soft tissue interfaces appear much sharper compared to $LPT(x, y)$ and $LPE(x, y)$ images. The final $LP(x, y)$ image shows the improvement achieved in terms of sensitivity to soft tissue artifacts and extraction of compact bone surfaces (Fig. 2f). The soft tissue interfaces are suppressed, while important bone surface responses are kept intact. In the next section, we explain how this enhanced local phase image ($LP(x, y)$) is used for the enhancement of bone shadow regions using US signal transmission maps.

Ultrasound transmission maps for enhancement of bone shadow region

The proposed US signal transmission map ($US_A(x, y)$) calculation, for bone shadow region enhancement, is based on the fact that the interaction of the US signal within the tissue can be modeled using the scattering and attenuation information. $US_A(x, y)$ maximizes the visibility of high-intensity features inside a local region and satisfies the constraint that the mean intensity of the local region is less than the echogenicity of the tissue confining the bone. This model was recently applied for the enhancement of needle shaft information from US data [31]. However, different from [31] our aim in this work is the enhancement of the shadow region rather than the needle interface.

In order to achieve this, the scattering and attenuation effects in the tissue are combined as:

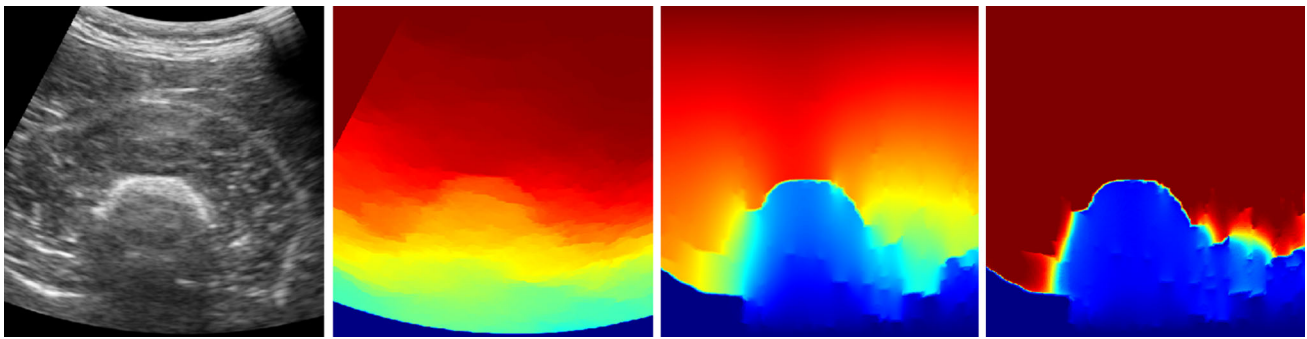


Fig. 3 Left to right B-mode US image of in vivo femur, $CM(x, y)$ image obtained using [25], $CM_{LP}(x, y)$ image, and $BSE(x, y)$ image

$$CM_{LP}(x, y) = US_A(x, y)BSE(x, y) + (1 - US_A(x, y))\rho. \quad (7)$$

Here, $CM_{LP}(x, y)$ is the CM image obtained from $LP(x, y)$ using [25], $US_A(x, y)$ is the signal transmission map, $BSE(x, y)$ is the enhanced bone shadow image and ρ is a constant value representative of echogenicity in the tissue surrounding the bone. Our aim is the extraction of $BSE(x, y)$ which is obtained by estimating the signal transmission map image $US_A(x, y)$. $US_A(x, y)$ is estimated by minimizing the following objective function [30,31]:

$$\begin{aligned} & \frac{\lambda}{2} \| US_A(x, y) - CM_{LP}(x, y) \|_2^2 \\ & + \sum_{j \in \chi} \| W_j \circ (D_j * US_A(x, y)) \|_1. \end{aligned} \quad (8)$$

Here, χ is an index set, \circ represents elementwise multiplication, and $*$ is convolution operator. D_j is obtained using a bank of high order differential filters consisting of eight Kirsch filters and one Laplacian filter [30]. The incorporation of this filter bank into the contextual regularization framework helps in further attenuating the image noise and results in the enhancement of ridge edge features such as the bone surface in the local region. W_j is a weighting matrix calculated using: $W_j(x, y) = \exp(-|D_j(x, y) * CM_{LP}(x, y)|^2)$. In Eq. 8, the first part is the data term which measures the dependability of $US_A(x, y)$ on $CM_{LP}(x, y)$. The second part of Eq. 8 models the contextual constraints of $US_A(x, y)$, and λ is the regularization parameter used to balance the two terms. The optimization of Eq. 8 is achieved using variable splitting where several auxiliary variables are introduced to construct a sequence of simple sub-problems, the solutions of which finally converge to the optimal solution of the original problem [30]. Once $US_A(x, y)$ is estimated, the enhanced bone shadow image $BSE(x, y)$ can be extracted using:

$$BSE(x, y) = [(CM_{LP}(x, y) - \rho) / [\max(US_A(x, y), \epsilon)]^\delta] + \rho. \quad (9)$$

Here, ϵ is a small constant used to avoid division by zero and δ is related to tissue attenuation coefficient (η) [31]. Investigating Fig. 3 we can see that the enhanced bone shadow image $BSE(x, y)$ has a uniform intensity region above the bone surface corresponding to the soft tissue interfaces representing a higher confidence values and shadow region is marked with uniform low-intensity values corresponding to a low confidence value (high intensity denoted with dark red and low intensity with blue color coding). Compared to $CM(x, y)$ image [25] and $CM_{LP}(x, y)$ image the transition from soft tissue interface to bone shadow region is sharper in the calculated $BSE(x, y)$ image.

Validation experiments

The US images used to evaluate the proposed method were obtained using an US system (SonixGPS, Analogic Corporation, Peabody, MA, USA) with a C5-2 curvilinear 2D probe. After obtaining the institutional review board (IRB) approval a total of 100 different US images were collected from five healthy subjects. For each subject, 10 femur and 10 lumbar spine scans were obtained. The image resolutions varied from 0.16 to 0.3 mm with depth settings between 8 and 16 cm. The proposed method was implemented using MATLAB 2014a software package and run on a 2.3 GHz Intel(R) Core™ i5 CPU, 16 GB RAM windows PC. The enhanced shadow region image ($BSE(x, y)$) was classified using k-means classification and the cluster corresponding to the maximum intensity cluster value was selected as the segmented region (Fig. 4b). Validation was performed against manually segmented shadow regions (Fig. 4b). Manual segmentation was performed by an expert user. Comparison against the previously proposed CM method [25] was also performed. During validation experiments, a region of interest (ROI) was selected which covered a bone interface spanning the full width of the image (Fig. 4b). $LPT(x, y)$ images were calculated using the filter parameter values defined in [19]. The ASSD filter parameters were: $sc = 2$, $\sigma = 25$ pixels, $a = 1.83$ and $\alpha = 0.2$. The $CM(x, y)$ and

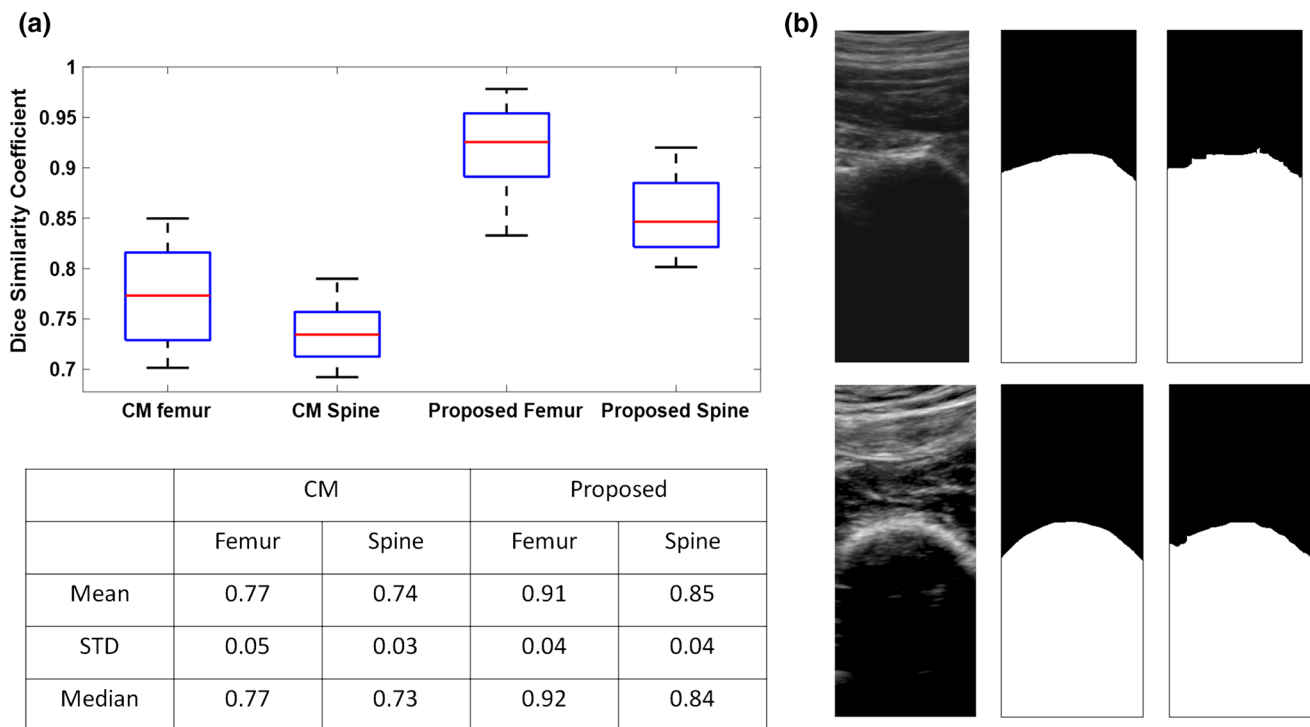


Fig. 4 **a** Quantitative results showing the calculated dice similarity coefficients for the CM method [25] and our proposed method. **b** ROI selected for the calculation of dice similarity coefficients. *Top from left to right* in vivo vertebra US image, manual shadow region segmentation result, shadow region segmented using the BSE(x, y) image as

an input to the k-means algorithm and selecting the highest intensity-valued cluster. *Bottom from left to right* in vivo femur US image, manual shadow region segmentation result, shadow region segmented using the BSE(x, y) image as an input to the k-means algorithm and selecting the highest intensity-valued cluster

$CM_{LP}(x, y)$ images were obtained using the constant values as: $\eta = 2$, $\beta = 90$, $\gamma = 0.03$. For Eq. 8, $\lambda = 2$ and ρ , the constant related to tissue echogenicity, was chosen as 90% of the maximum intensity value of $CM_{LP}(x, y)$. These values were determined empirically and kept constant during qualitative and quantitative analysis.

Results

The calculated dice coefficients for different bone surfaces are shown in Fig. 4. The overall mean dice similarity coefficient for the proposed method was 0.88 (STD 0.05) compared to 0.75 (STD 0.04) for the state-of-the-art method proposed in [25]. The mean computation time was 9.3 seconds, for an entire image, with an un-optimized MATLAB code. Investigating the box and whisker plots we can see that proposed method was more successful for identification of shadow regions from femur bone scans compared to vertebra bone scans (Fig. 4a). This is an expected result since the spine bone surfaces have a more irregular 3D shape and surrounded by ligaments which makes the surface response profile have a more irregular shape compared to femur surface response. Qualitative evaluation results present the improvement achieved, for bone shadow detection, with the

proposed method compared to the CM method [25] (Figs. 5, 6). The separation of shadow region from the soft tissue interface is more distinct with less intensity variations for soft tissue layers (Figs. 5, 6).

Discussions and conclusions

The success of US-guided CAOS procedures depends on the quality of the intra-operatively obtained US data and the subsequent accurate localization of bone surfaces. Shadow region is an important feature, present in all of the collected US scans indicating the presence of a bone surface. Consequently, it has been incorporated as an additional feature into many bone segmentation and localization methods to improve the robustness. In this work, we present a method based on the combination of three different local phase features for enhancement of bone/tissue interfaces and the consecutive detection of bone shadow regions using a weighted L_1 norm-based contextual regularization. We compared our results with previously published approach [25]. Quantitative validation achieved an improvement of around 18% for femur bone shadow enhancement, and 15% for vertebra bone shadow enhancement compared to state-of-the-art method [25].

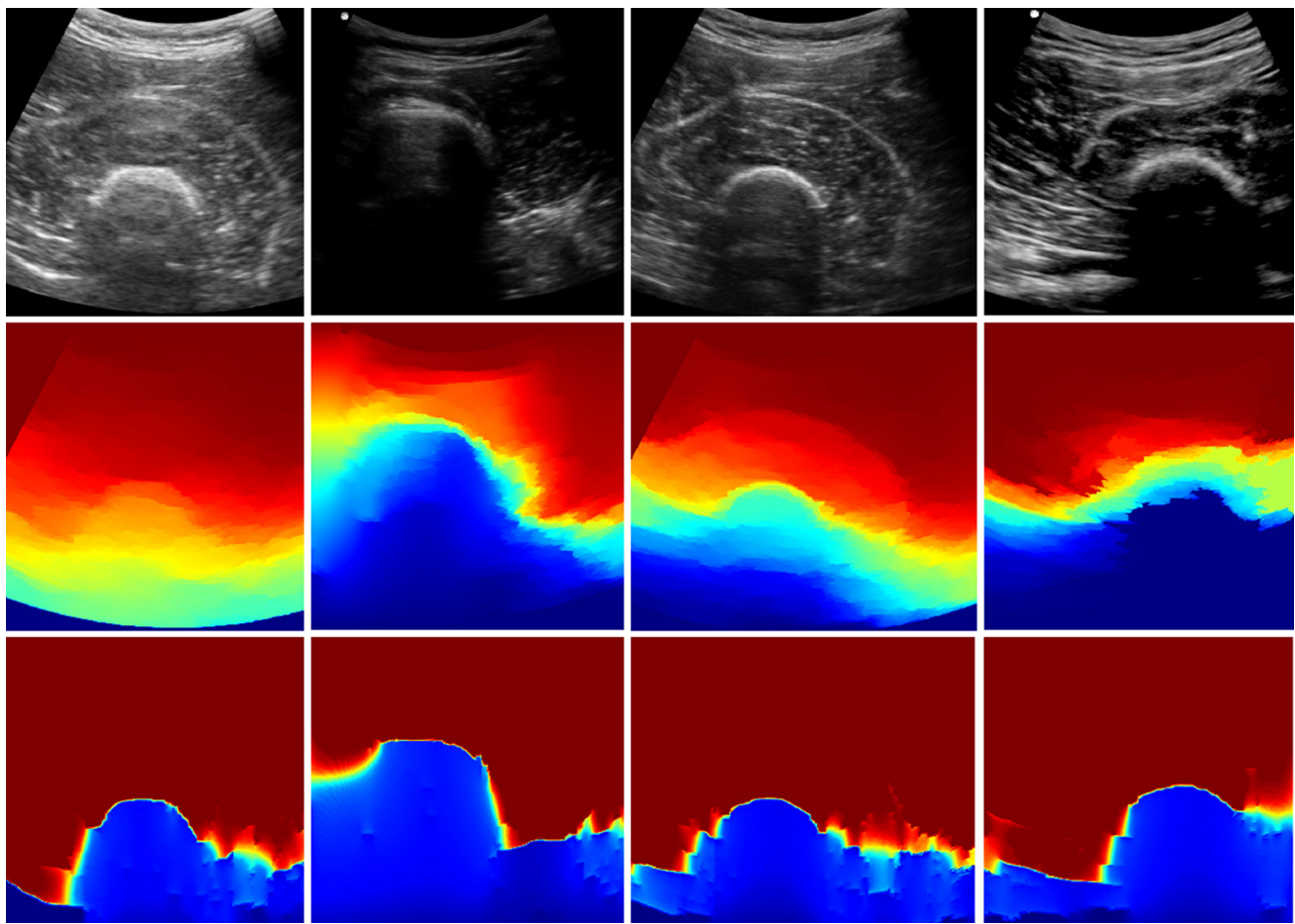


Fig. 5 Qualitative results obtained from in vivo scanning of femur bone. *Top row* B-mode US images. *Middle row* $CM(x, y)$ images obtained using the method proposed in [25]. *Bottom row* enhanced bone shadow images $BSE(x, y)$

One of the limitations of our method is the computation time which is around 9 seconds. Real-time guidance is important in US-based CAOS systems. Therefore, an improvement in the computation time needs to be achieved before incorporating the proposed method into a guidance system as an additional feature. However, graphics processing unit (GPU)-accelerated image processing algorithms have been developed for various applications [11,36]. Therefore, we believe that GPU implementation of the proposed method will achieve the required computation time for real-time guidance. The proposed method requires the selection of different filter and regularization parameters which were selected empirically for this work and kept constant during the validation. However, a more comprehensive analysis is required in order to relate these parameter choices to the properties of the acquired US images and the following image processing task. Figure 7 shows different $BSE(x, y)$ images obtained by changing the value of the λ parameter used during the regularization. Investigating the $BSE(x, y)$ images, we can see that the λ parameter impacts more the transi-

tion interface from soft tissue response to the bone shadow region (lateral direction) and has a minimal impact for the bone surface response to shadow region transition section (axial direction). This change might impact the segmentation or registration methods if the $BSE(x, y)$ images are used for these tasks which requires further investigation. Finally, the validation experiments were conducted by selecting a ROI which was performed by an expert user. Despite the fact that the user did not have access to the $BSE(x, y)$ images during this process intra- and inter-user variability for the ROI selection process should be performed in order to fully understand the bias involved during the ROI selection.

Future work will focus on further validation of the proposed method on more clinical datasets obtained in vivo. One of the limitations of US imaging is the limited field of view. In order to overcome this extended field of view US imaging has been proposed. Consequently, we are also interested in validating our method on extended field of view US datasets. Finally, we will also validate the method on different

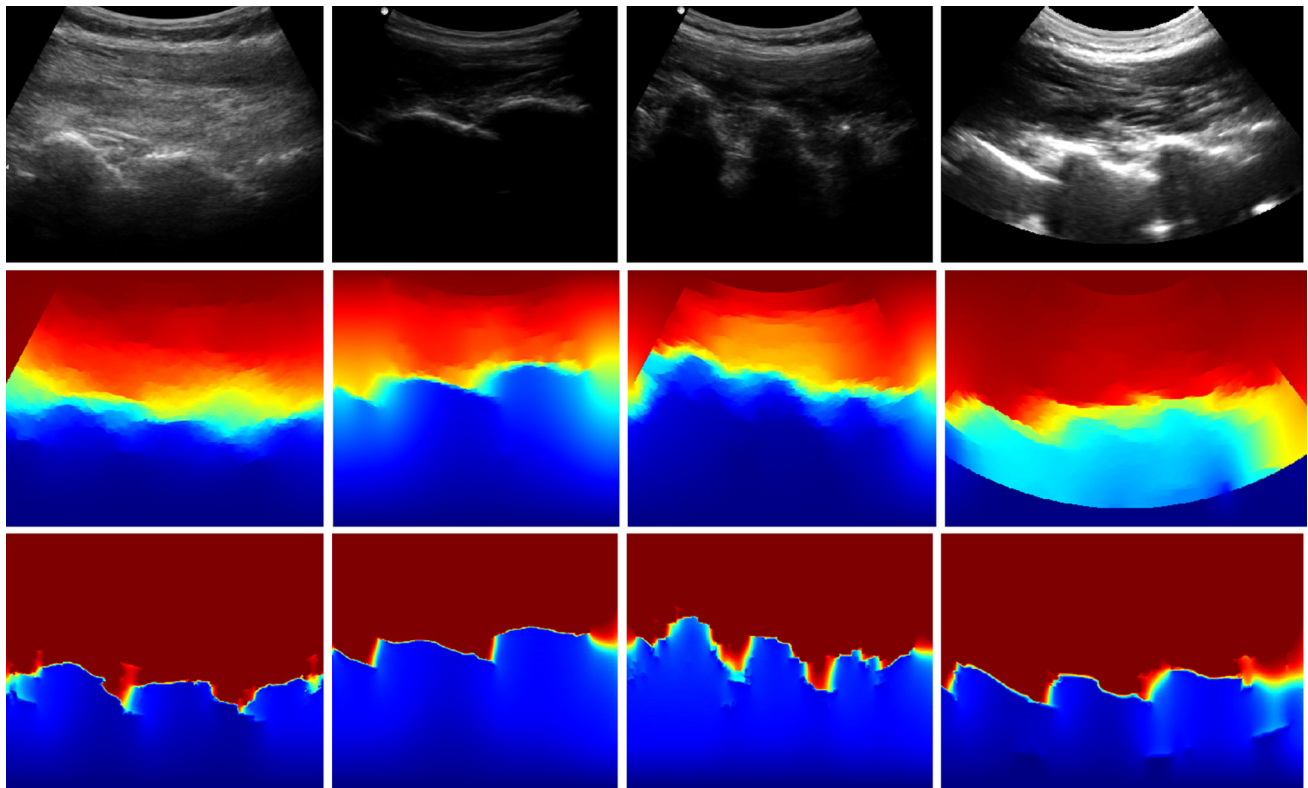


Fig. 6 Qualitative results obtained from in vivo scanning of vertebrae bone. *Top row* B-mode US images. *Middle row* $CM(x, y)$ images obtained using the method proposed in [25]. *Bottom row* enhanced bone shadow images $BSE(x, y)$

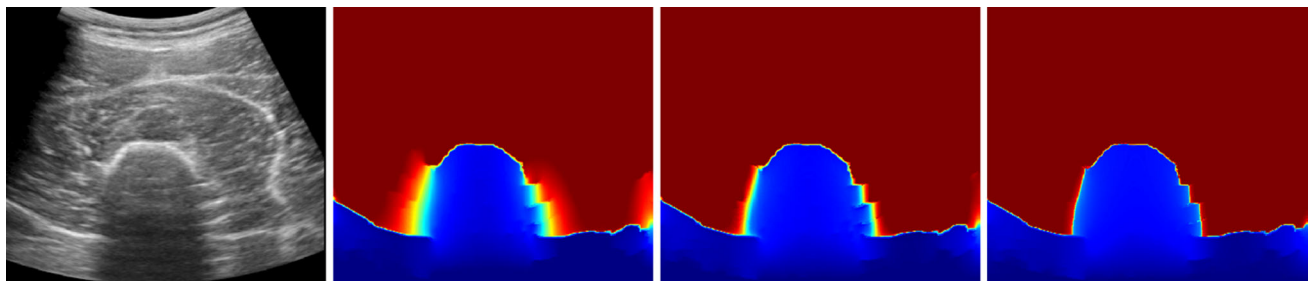


Fig. 7 Regularization results obtained using different λ values. *From left to right* In vivo US image, $BSE(x, y)$ obtained using $\lambda = 0.2$, $BSE(x, y)$ obtained using $\lambda = 2$, $BSE(x, y)$ obtained using $\lambda = 200$

segmentation and registration approaches and investigate the potential of the method for improving the registration robustness.

Compliance with ethical standards

Ethical approval All procedures performed in studies involving human participants were in accordance with the ethical standards of the institutional and/or national research committee and with the 1964 Helsinki Declaration and its later amendments or comparable ethical standards.

References

1. Amin DV, Kanade T, Digioia AM, Jaramaz B (2003) Ultrasound registration of the bone surface for surgical navigation. *Comput Aided Surg* 8(1):1–16
2. Anas EMA, Seitel A, Rasoulia A, John PS, Pichora D, Darras K, Wilson D, Lessoway VA, Hacıhaliloglu I, Mousavi P, Rohling R, Abolmaesumi P (2015) Bone enhancement in ultrasound using local spectrum variations for guiding percutaneous scaphoid fracture fixation procedures. *Int J Comput Assist Radiol Surg* 10(6):959–969
3. Anas EMA, Seitel A, Rasoulia A, John PS, Ungi T, Lasso A, Darras K, Wilson D, Lessoway VA, Fichtinger G, Rohling R, Abolmaesumi P (2016) Bone enhancement in ultrasound based on 3d local spectrum variation for percutaneous scaphoid fracture fixation. In: *International conference on medical image computing and computer-assisted intervention*. Springer, pp 465–473
4. Barratt DC, Penney GP, Chan CS, Slomczykowski M, Carter TJ, Edwards PJ, Hawkes DJ (2006) Self-calibrating 3d-ultrasound-based bone registration for minimally invasive orthopedic surgery. *IEEE Trans Med Imaging* 25(3):312–323
5. Beek M, Abolmaesumi P, Luenam S, Ellis RE, Sellens RW, Pichora DR (2008) Validation of a new surgical procedure for percutaneous

- scaphoid fixation using intra-operative ultrasound. *Med Image Anal* 12(2):152–162
6. Belaid A, Boukerroui D (2014) α scale spaces filters for phase based edge detection in ultrasound images. In: 2014 IEEE 11th international symposium on biomedical imaging (ISBI). IEEE, pp 1247–1250
 7. Berton F, Cheriet F, Miron MC, Laporte C (2016) Segmentation of the spinous process and its acoustic shadow in vertebral ultrasound images. *Comput Biol Med* 72:201–211
 8. Brendel B, Winter S, Rick A, Stockheim M, Ermer H (2002) Registration of 3d CT and ultrasound datasets of the spine using bone structures. *Comput Aided Surg* 7(3):146–155
 9. Brounstein A, Hacıhaliloglu I, Guy P, Hodgson A, Abugharbieh R (2015) Fast and accurate data extraction for near real-time registration of 3-d ultrasound and computed tomography in orthopedic surgery. *Ultrasound Med Biol* 41(12):3194–3204
 10. Chen TK, Abolmaesumi P, Pichora DR, Ellis RE (2005) A system for ultrasound-guided computer-assisted orthopaedic surgery. *Comput Aided Surg* 10(5–6):281–292
 11. Chung J, Daoud MI, Imani F, Mousavi P, Abolmaesumi P (2012) Gpu accelerated implementation of ultrasound radio-frequency time series analysis. In: SPIE Medical imaging. International Society for Optics and Photonics, pp 83,2011–83,2011
 12. Daanen V, Tonetti J, Troccaz J (2004) A fully automated method for the delineation of osseous interface in ultrasound images. In: International conference on medical image computing and computer-assisted intervention. Springer, pp 549–557
 13. Felsberg M, Köthe U (2005) Get: The connection between monogenic scale-space and gaussian derivatives. In: International conference on scale-space theories in computer vision. Springer, pp 192–203
 14. Felsberg M, Sommer G (2000) A new extension of linear signal processing for estimating local properties and detecting features. In: Mustererkennung 2000. Springer, pp 195–202
 15. Felsberg M, Sommer G (2001) The monogenic signal. *IEEE Trans Signal Process* 49(12):3136–3144
 16. Foroughi P, Boctor E, Swartz MJ, Taylor RH, Fichtinger G (2007) P6d-2 ultrasound bone segmentation using dynamic programming. In: Ultrasonics symposium, 2007. IEEE, pp 2523–2526. IEEE
 17. Hacıhaliloglu I, Abugharbieh R, Hodgson AJ, Rohling RN (2009) Bone surface localization in ultrasound using image phase-based features. *Ultrasound Med Biol* 35(9):1475–1487
 18. Hacıhaliloglu I, Guy P, Hodgson AJ, Abugharbieh R (2015) Automatic extraction of bone surfaces from 3d ultrasound images in orthopaedic trauma cases. *Int J Comput Assist Radiol Surg* 10(8):1279–1287
 19. Hacıhaliloglu I, Rasoulia A, Rohling RN, Abolmaesumi P (2014) Local phase tensor features for 3-d ultrasound to statistical shape+ pose spine model registration. *IEEE Trans Med Imaging* 33(11):2167–2179
 20. Hacıhaliloglu I, Wilson DR, Gilbert M, Hunt MA, Abolmaesumi P (2013) Non-iterative partial view 3d ultrasound to ct registration in ultrasound-guided computer-assisted orthopedic surgery. *Int J Comput Assist Radiol Surg* 8(2):157–168
 21. Hott JS, Deshmukh VR, Klopfenstein JD, Sonntag VK, Dickman CA, Spetzler RF, Papadopoulos SM (2004) Intraoperative iso-c arm navigation in craniocervical surgery: the first 60 cases. *Neurosurgery* 54(5):1131–1137
 22. Jain AK, Taylor RH (2004) Understanding bone responses in b-mode ultrasound images and automatic bone surface extraction using a Bayesian probabilistic framework. In: Medical imaging 2004. International Society for Optics and Photonics, pp. 131–142
 23. Jaramaz B, DiGioia AM III, Blackwell M, Nikou C (1998) Computer assisted measurement of cup placement in total hip replacement. *Clin Orthop Relat Res* 354:70–81
 24. Jia R, Mellon SJ, Hansjee S, Monk A, Murray D, Noble JA (2016) Automatic bone segmentation in ultrasound images using local phase features and dynamic programming. In: 2016 IEEE 13th international symposium on biomedical imaging (ISBI). IEEE, pp 1005–1008
 25. Karamalis A, Wein W, Klein T, Navab N (2012) Ultrasound confidence maps using random walks. *Med Image Anal* 16(6):1101–1112
 26. Klein T, Wells III WM (2015) Rf ultrasound distribution-based confidence maps. In: International conference on medical image computing and computer-assisted intervention. Springer, pp 595–602
 27. Kowal J, Amstutz C, Langlotz F, Talib H, Ballester MG (2007) Automated bone contour detection in ultrasound b-mode images for minimally invasive registration in computer-assisted surgery in vitro evaluation. *Int J Med Robot Comput Assist Surg* 3(4):341–348
 28. Laine T, Schlenzka D, Mäkitalo K, Tallroth K, Nolte LP, Viisari H (1997) Improved accuracy of pedicle screw insertion with computer-assisted surgery: a prospective clinical trial of 30 patients. *Spine* 22(11):1254–1258
 29. Linsenmaier U, Rock C, Euler E, Wirth S, Brandl R, Kotsianos D, Mutschler W, Pfeifer KJ (2002) Three-dimensional ct with a modified c-arm image intensifier: feasibility 1. *Radiology* 224(1):286–292
 30. Meng G, Wang Y, Duan J, Xiang S, Pan C (2013) Efficient image dehazing with boundary constraint and contextual regularization. In: Proceedings of the IEEE international conference on computer vision, pp 617–624
 31. Mwikirize C, Noshier JL, Hacıhaliloglu I (2016) Enhancement of needle tip and shaft from 2d ultrasound using signal transmission maps. In: International conference on medical image computing and computer-assisted intervention. Springer, pp 362–369
 32. Nieves J, Bilezikian J, Lane J, Einhorn T, Wang Y, Steinbuch M, Cosman F (2010) Fragility fractures of the hip and femur: incidence and patient characteristics. *Osteoporos Int* 21(3):399–408
 33. Ozdemir F, Ozkan E, Goksel O (2016) Graphical modeling of ultrasound propagation in tissue for automatic bone segmentation. In: International conference on medical image computing and computer-assisted intervention. Springer, pp 256–264
 34. Quader N, Hodgson A, Abugharbieh R (2014) Confidence weighted local phase features for robust bone surface segmentation in ultrasound. In: Workshop on clinical image-based procedures. Springer, pp 76–83
 35. Rajaei SS, Bae HW, Kanim LE, Delamarter RB (2012) Spinal fusion in the united states: analysis of trends from 1998 to 2008. *Spine* 37(1):67–76
 36. Reichl T, Passenger J, Acosta O, Salvado O (2009) Ultrasound goes GPU: real-time simulation using CUDA. In: SPIE medical imaging. International Society for Optics and Photonics, pp 116–126
 37. Saragaglia D, Picard F, Chaussard C, Montbarbon E, Leitner F, Cinquin P (2001) [computer-assisted knee arthroplasty: comparison with a conventional procedure. Results of 50 cases in a prospective randomized study]. *Rev Chir orthop Reparat l'appar Mot* 87(1):18–28
 38. Słomczykowski MA, Hofstetter R, Sati M, Krettek C, Nolte LP (2001) Novel computer-assisted fluoroscopy system for intraoperative guidance: feasibility study for distal locking of femoral nails. *J Orthop Trauma* 15(2):122–131
 39. Stöckle U, König B, Schäffler A, Zschoernack T, Haas N (2006) Clinical experience with the siremobil iso-c (3d) imaging system in pelvic surgery. *Unfallchirurg* 109(1):30–40
 40. Yan CX, Goulet B, Pelletier J, Chen SJS, Tampieri D, Collins DL (2011) Towards accurate, robust and practical ultrasound-CT reg-

- istration of vertebrae for image-guided spine surgery. *Int J Comput Assist Radiol Surg* 6(4):523–537
41. Zheng G, Nolte LP (2015) Computer-assisted orthopedic surgery: current state and future perspective. *Front Surg* 2(66):1–14